Transport in Porous Media (2020) 132:657–681
https://doi.org/10.1007/s11242-020-01407-y

Conjugate Phase Change Heat Transfer in an Inclined Compound Cavity Partially Filled with a Porous Medium: A Deformed Mesh Approach

S. A. M. Mehryan[1] · Kasra Ayoubi-Ayoubloo[2] · Mohammad Shahabadi[3] · Mohammad Ghalambaz[4,5] · Pouyan Talebizadehsardari[6,5] · Ali Chamkha[7]

Received: 1 December 2019 / Accepted: 12 March 2020 / Published online: 1 April 2020

Abstract
In this paper, the melting process of a PCM inside an inclined compound enclosure partially filled with a porous medium is theoretically addressed using a novel deformed mesh method. The sub-domain area of the compound enclosure is made of a porous layer and clear region. The right wall of the enclosure is adjacent to the clear region and is subject to a constant temperature of T_c. The left wall, which is connected to the porous layer, is thick and thermally conductive. The thick wall is partially subject to the hot temperature of T_h. The remaining borders of the enclosure are well insulated. The governing equations for flow and heat transfer, including the phase change effects and conjugate heat transfer at the thick wall, are introduced and transformed into a non-dimensional form. A deformed grid method is utilized to track the phase change front in the solid and liquid regions. The melting front movement is controlled by the Stefan condition. The finite element method, along with Arbitrary Eulerian–Lagrangian (ALE) moving grid technique, is employed to solve the non-dimensional governing equations. The modeling approach and the accuracy of the utilized numerical approach are verified by comparison of the results with several experimental and numerical studies, available in the literature. The effect of conjugate wall thickness, inclination angle, and the porous layer thickness on the phase change heat transfer of PCM is investigated. The outcomes show that the rates of melting and heat transfer are enhanced as the thickness of the porous layer increases. The melting rate is the highest when the inclination angle of the enclosure is 45°. An increase in the wall thickness improves the melting rate.

Keywords Phase change materials (PCMs) · Porous layer · ALE moving grid · Compound enclosure · Finite element method

✉ Mohammad Ghalambaz
mohammad.ghalambaz@tdtu.edu.vn

✉ Pouyan Talebizadehsardari
ptsardari@tdtu.edu.vn

Extended author information available on the last page of the article

List of Symbols

Latin symbols

A	Area
$A_{s,i}$	Scaled absolute tolerance for degrees of freedom i
C_p	Specific heat capacity
d	Wall length
Da	Darcy number
E_Y	Estimate of the local error (absolute error)
g	Gravitational acceleration
k	Thermal conductivity
L	Cavity length
M	Number of fields
N_j	Number of degrees of freedom in a field
Pr	Prandtl number
R	Relative tolerance
Ra	Rayleigh number
s	Porous media length
Ste	Stefen number
t	Dimensional time
T	Dimensional temperature
u, v	Components of dimensional velocity along x and y directions
U, V	Components of non-dimensional velocity along x and y velocity
x, y	Dimensional cartesian coordinates
X, Y	Non-dimensional cartesian coordinatess
Y_i	Scaled solution vector

Greek Symbols

α	Thermal diffusivity
β	Volume expansion coefficient
γ	Inclination angle
ε	Porosity
ζ	Basis function
θ	Dimensionless temperature
ν_f	Kinematic viscositys
ρ	Density
τ	Dimensionless time

Subscripts

c	Cold
h	Hot
i, j	Degrees of freedom, field number
l	Liquid
m	Melt
p	Property of metal foam
s	Solid
w	Wall

1 Introduction

Phase change materials (PCMs) are a decent choice for thermal energy storage plans such as solar power, electrical vehicles cooling systems, and waste heat recovery. PCMs can store/release a tremendous amount of energy on the phase change at a constant temperature. The latent heat of PCMs can be achieved by solid–solid, solid–liquid, solid–gas, and liquid–gas phase changes; however, solid–liquid and liquid–gas phase changes are more convenient to manage for thermal energy storage applications.

The importance of solidification and melting processes has contributed to huge scientific endeavors by numerical, experimental, and analytical investigations up to date (Kumar et al. 2012; Wang et al. 2019a; Bondareva et al. 2019; Bondareva and Sheremet 2018). There are some recent works that have studied new aspects of phase change heat transfer in clear regions such as using a magnetic field, nanoadditives, or fins. For example, Ghalambaz et al. (2017b) studied the effects of a magnetic field and inclination angle of an enclosure on the melting process of hydrodynamic magnetic phase change phenomena. Results showed that the magnetic field could decrease the thermal gradient in the enclosure by weakening the natural convection effects. Doostani et al. (2017) numerically investigated the effect of using a uniform magnetic field on the melting process of an electrically conductive PCM. Results indicated that at an early stage of the melting process, in which the flow velocity is low, the magnetic field has a slight impact on the melting rate and phase change behavior. Chamkha et al. (2017) studied the influence of using nanoadditives on the phase change behavior of PCMs in a horizontal cylindrical enclosure. Results showed that the interface of solid–liquid was affected by nanoparticles volume fraction. Ghalambaz et al. (2017a) investigated the effect of using hybrid nanoparticles as nanoadditives on the natural convection melting process inside an enclosure. The results indicated that a stable dispersion of nanoparticles inside the PCMs led to the augmentation of heat conduction in comparison with the base fluid PCMs. Tiari et al. (2015) conducted numerical studies on a thermal finned tube equipped with a thermal energy storage system with high-temperature PCMs inside a quadratic enclosure. Results showed that natural convection had a significant effect on the melting process of PCMs. Khodadadi and Hoseinizadeh (2007) studied the improvement of phase change heat transfer of PCMs by adding nanoparticles. They enhanced the heat conduction of PCM by introducing nanoparticle as additives to synthesize an enhanced phase change substance. Fan and Khodadadi (2011) reviewed the recent advances in the experimental and numerical simulations of phase change heat transfer of PCMs.

The study of the literature review shows that various enclosure shapes and conditions have been utilized as a container for phase change materials (PCMs). Hlimi et al. (2016) numerically investigated the role of natural convection on the melting phase change inside a horizontal cylinder. They utilized the enthalpy–porosity method to model the phase change, and they found that the natural convection played an essential role in the melting shape and temperature of PCM.

Faghani et al. (2018) numerically surveyed the melting process between elliptical cylinders in nine different configurations. RT 25 (Rubitherm Gmbh—Germany) was used as the PCM filling between the inner and outer ellipses. Results revealed that a horizontal elliptical tube shows the best performance to be used as a shell. Rakotondrandisa et al. (2019) carried out numerical studies to simulate the melting and solidification process of a PCM. The enthalpy method was applied to the energy equation. They investigated the solidification of octadecane paraffin after a partial melting (around 50%).

Elsayed (2018) numerically studied the melting characteristics of commercial paraffin wax as PCM inside triangular cylinder containers. The cylinders had the same volume and various apex angles which their effects on heat transfer and flow pattern were provided. The results revealed that the base length and apex angle of the triangle considerably affect the heat storage efficiency and the container surface.

Wang et al. (2019b) conducted experiments to study the melting process of PCM inside a cylindrical container with various boundary conditions. According to the experimental results of this study, the initial melting process occurred based on the conduction heat transfer mechanism, and after empowering natural convection, it became the predominant cause of melting. Bechiri and Mansouri (2019) carried out numerical studies on the melting process in a vertical cylindrical tube partially filled with PCM and air. They provided correlations for the melted liquid fraction and time of melting based on dimensionless parameters such as Fourier and Grashof numbers.

Using high thermal conductive porous materials is a novel approach to enhance or control the phase change of PCMs. Recently, the methods and techniques for the design of various metal foams have significantly advanced. Zhao et al. (2018) performed an excellent review on the applications of metal foams. Hence, a large number of researchers studied the impacts of using a porous medium on the flow and heat transfer of the fluids without phase change (Mehryan et al. 2019b; Ghalambaz et al. 2016; Pop et al. 2016; Chamkha and Selimefendigil 2018; Nield and Bejan 2006; Alsabery et al. 2019c).

Ghalambaz et al. (2016) studied the free convection flow inside a quadratic enclosure occupied with porous media and saturated with nanofluid by considering the viscous dissipations and effects of radiation. Pop et al. (2016) investigated free convection in a quadratic porous cavity occupied with nanofluid by thermal non-equivalent and Buongiorno model. Mehryan et al. (2019b) studied the impacts of the presence of the foam on the flow and heat transfer of a suspension containing hybrid nanoparticles. Sheikholeslami (2019a,b) investigated the free convection of nanofluids in a cavity with no phase change by using a combination of finite element and finite volume methods. The lattice Boltzmann has also been applied for the investigation of natural convection of nanofluids with no phase change (Sheikholeslami et al. 2019b).

The phase change heat transfer in porous media has been investigated in some of the recent works. Jourabian et al. (2018b) conducted numerical investigations to accelerate the melting process by using metallic porous media. The enthalpy-based lattice Boltzmann method was employed. The results showed that using this porous media contributes to the enhancement of conduction and the weakening of natural convection heat transfer. Jourabian et al. (2018a) investigated the melting rate inside two configurations of cylinders: one cylinder and four cylinders with three different configurations. The PCM used in this research was mixed with the small volumetric concentration of the nanometer-sized Cu particles to enhance the melting rate. Results revealed that the melting time in a single tube with pure PCM was higher than the multi-tube configuration with pure PCM and nanoenhanced phase change material (NEPCM) melting in a multi-tube configuration. Also, different arrays had a different time of melting. Al-Jethelah et al. (2016) numerically and analytically performed an analysis of the melting process inside a porous square enclosure.

Al-Jethelah et al. (2016) found that the flow of melted PCM and the melting front are significantly affected by the Darcy and porosity numbers. Hayat et al. (2017) utilized the boundary layer analysis to study the melting heat transfer in a stagnation point flow. The free convection in a cavity with no phase change has also been the subject of many recent studies, for instance conjugate heat transfer effects (Alsabery et al. 2018b, 2019a,b), wavy

wall geometry effects (Alsabery et al. 2018a,2019b,c), double-diffusive effects (Ismael 2018; Ismael and Ghalib 2018), and magnetic field effects (Alsabery et al. 2018c, 2019a).

Considering the compound enclosure, Tahmasebi et al. (2018) investigated the conjugate natural convection heat transfer in an enclosure partially filled with a layer of porous medium for a homogeneous nanofluid. Mehryan et al. (2019a) extended the study of Tahmasbei et al. (2018) to the case of a non-homogeneous nanofluid. Hu et al. (2018) also extended the study of Tahmasebi et al. (2018) to the case of double-diffusive natural convection. The geometry of a cavity with a layer of porous medium with no phase change has also been investigated in Sheremet et al. (2019).

The conventional method for modeling of phase change heat transfer is the enthalpy–porosity method. In this method, it is presumed the phase change takes place in a range of temperature instead of an exact temperature to avoid discontinuity in the heat equation (Doostani et al. 2017; Chamkha et al. 2017; Sheikholeslami et al. 2019a; Sheikholeslami 2018a, b, c). The deformed mesh method benefits from the moving grid capability for tracking of phase change interface, and hence, the phase change can be tracked with an exact fusion temperature.

The literature review shows that the natural convection with no phase change has been studied inside a compound cavity, including the wall, porous layer, and clear region in recent years (Tahmasebi et al. 2018; Mehryan et al. 2019a; Hu et al. 2018). However, the melting heat transfer in a compound enclosure has not been addressed yet. The present study aims to analyze the effects of wall thickness and porous layer on the melting rate of a phase change material using a novel deformed grid method for the first time. The deformed mesh method is employed to capture phase change at an exact fusion temperature, accurately.

2 Modeling

Figure 1 demonstrates the schematic diagram for conjugate natural convection of the melting process in a compound enclosure with a layer of a porous medium. The enclosure is a rectangular domain with the height of L and the width of $L+s$. The enclosure is vertically separated into three sections: a solid wall, a porous medium, and a clear flow region. The solid and the porous areas are defined by s and d, respectively. It is worth mentioning that the width of the porous layer and the clear region is considered to be constant. As pictured in Fig. 1, a flash heater having a hot temperature of T_h and length of b is mounted on the left wall with the central position height of z. The entire right surface of the enclosure is subject to a fixed temperature of T_c so that $T_c < T_h$. The remaining surfaces of the compound enclosure are well insulated.

For modeling the conjugate natural convection of the PCM, the following points need to be explained. The condition of the no-slip boundary is established on the solid surfaces. The pores of the porous region are fully occupied by an incompressible liquid/solid PCM. The pores are homogeneously distributed, and the solid matrix is assumed to be isotropic. Aluminum metal foam and paraffin wax are selected as the solid matrix and the PCM. The thermal properties are provided in Tables 1 and 2. The constructive material of the wall and the porous medium are similar, and hence, the thermophysical properties in Table 2 are also applicable for the solid wall. Besides, the flow of molten PCM is Newtonian and laminar. Apart from density in the buoyancy term, all

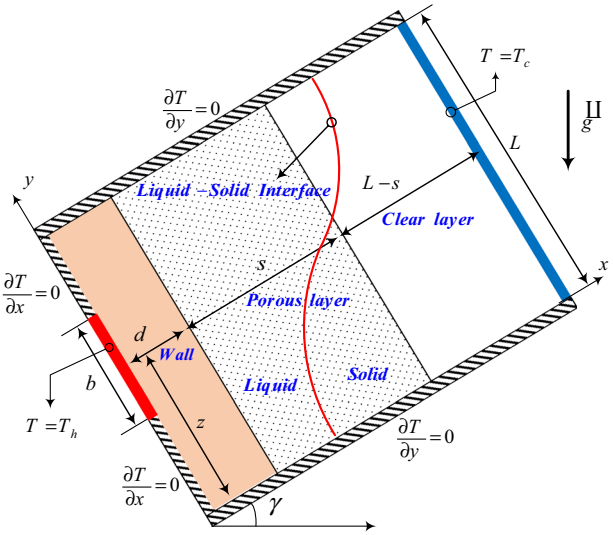

Fig. 1 Schematic view of the physical model

Table 1 Properties of the liquid and solid paraffin wax (Farid et al. 2004)

The property, symbol (unit)	Solid	Liquid
Thermal conductivity, k_s and k_l [W/(m K)]	0.23	0.2
Specific heat, $C_{p,s}$ and $C_{p,l}$ [kJ/(kg K)]	2.20	2.10
Latent heat of melting, L_{fs} (kJ/kg)	190	190
Liquid temperature, T_l (°C)	–	59.9
Solidus temperature, T_s (°C)	51.2	–
Kinematic viscosity, ν (m/s^2)	–	5.2×10^{-6}
Thermal diffusivity, α (m/s^2)	1.2672×10^{-7}	1.2614×10^{-7}
Density, ρ_s and ρ_l (kg/m)	825	755
Liquid thermal expansion coefficient, β [1/ C]	–	4.016×10^{-3}

Density, specific heat and thermal conductivity used in the numerical model are considered at 59.9 °C.

Table 2 Thermal and physical properties of the metal foam (Dinesh and Bhattacharya 2019)

The property, symbol (unit)	Value
Thermal conductivity, k_p [W/(m K)]	205
Specific heat, $C_{p,p}$ [kJ/(kg K)]	0.910
Density, ρ_p (kg/m)	2830

the thermophysical characteristics of the liquid/solid PCM are regarded as constant. The Boussinesq approximation is utilized to take into account the impacts of the buoyancy volume force.

Taking into account the points mentioned above, a set of governing equations describing the molten PCM flow and heat transfer in the free and porous regions are written as follows (Nield and Bejan 2006; Buongiorno 2006; Sheikholeslami et al. 2018):

$$\frac{\partial u}{\partial x}+\frac{\partial v}{\partial y}=0 \tag{1}$$

$$\frac{\rho}{\varepsilon}\frac{\partial u}{\partial t}+\frac{\rho}{\varepsilon^2}\left(u\frac{\partial u}{\partial x}+v\frac{\partial u}{\partial y}\right)=-\frac{\partial p}{\partial x}+\frac{\mu}{\varepsilon}\left(\frac{\partial^2 u}{\partial x^2}+\frac{\partial^2 u}{\partial y^2}\right)-\frac{\mu}{K}u+\rho g\beta\left(T_l-T_f\right)\sin(\gamma) \tag{2}$$

$$\frac{\rho}{\varepsilon}\frac{\partial v}{\partial t}+\frac{\rho}{\varepsilon^2}\left(u\frac{\partial v}{\partial x}+v\frac{\partial v}{\partial y}\right)=-\frac{\partial p}{\partial y}+\frac{\mu}{\varepsilon}\left(\frac{\partial^2 v}{\partial x^2}+\frac{\partial^2 v}{\partial y^2}\right)-\frac{\mu}{K}v+\rho g\beta\left(T_l-T_f\right)\cos(\gamma) \tag{3}$$

Energy balance for the melted PCM:

$$(\rho C_p)_{m,l}\frac{\partial T_l}{\partial t}+(\rho C_p)_l\left(u\frac{\partial T_l}{\partial x}+v\frac{\partial T_l}{\partial y}\right)=k_{m,l}\left(\frac{\partial^2 T_l}{\partial x^2}+\frac{\partial^2 T_l}{\partial y^2}\right) \tag{4}$$

where

$$\begin{aligned}(\rho C_p)_{m,l}&=(1-\varepsilon)(\rho C_p)_p+\varepsilon(\rho C_p)_l\\ k_{m,l}&=(1-\varepsilon)k_p+\varepsilon k_l\end{aligned} \tag{5}$$

Energy balance for solid PCM:

$$(\rho C_p)_{m,s}\frac{\partial T_s}{\partial t}=k_{m,s}\left(\frac{\partial^2 T_s}{\partial x^2}+\frac{\partial^2 T_s}{\partial y^2}\right) \tag{6}$$

where

$$\begin{aligned}(\rho C_p)_{m,s}&=(1-\varepsilon)(\rho C_p)_p+\varepsilon(\rho C_p)_s\\ k_{m,s}&=(1-\varepsilon)k_p+\varepsilon k_s\end{aligned} \tag{7}$$

In the clear space, $\varepsilon\to 1$ and $K\to\infty$. So, the porous layer can be defined as $\varepsilon=\varepsilon\,\mathrm{step}(x)+(1-\mathrm{step}(x))$ and $K=K\,\mathrm{step}(x)+\infty\times(1-\mathrm{step}(x))$ where ∞ is a large number order of 10^2 and step function is defined as follows:

$$\mathrm{step}(x)=\begin{cases}1 & d<x<s\\ 0 & x>s\end{cases} \tag{8}$$

Energy balance for the solid wall:

$$\left(\rho C_p\right)_w\frac{\partial T_w}{\partial t}=k_w\left(\frac{\partial^2 T_w}{\partial x^2}+\frac{\partial^2 T_w}{\partial y^2}\right) \tag{9}$$

The imposed boundary conditions to the physics are:
On the wall–porous interface:

$$\begin{aligned}&T_w\big|_{wall}=T\big|_{porous}\\ &k_w\frac{\partial T_w}{\partial n}\bigg|_{wall}=k_{m,l}\frac{\partial T}{\partial n}\bigg|_{porous}\ or\ k_w\frac{\partial T_w}{\partial n}\bigg|_{wall}=k_{m,s}\frac{\partial T}{\partial n}\bigg|_{porous}\end{aligned} \tag{10}$$

On the external surfaces:

$$\begin{cases} T_w(0,y) = T_h & z - b/2 \le y \le z + b/2 \\ \frac{\partial T_w(0,y)}{\partial x} = 0 & y \ge z + b/2 \,\&\, y \le z - b/2 \end{cases}$$
$$u(L,y) = v(L,y) = 0, \quad T(L,y) = T_c$$
$$u(x,0) = v(x,0) = 0, \quad \frac{\partial T_w(x,0)}{\partial y} = \frac{\partial T(x,0)}{\partial y} = 0 \tag{11}$$
$$u(x,L) = v(x,L) = 0, \quad \frac{\partial T_w(x,L)}{\partial y} = \frac{\partial T(x,L)}{\partial y} = 0$$

In the present study, the porous layer and the clear flow regions are separated through the change in porosity and permeability using a step function. Please see Eq. (8) and the text above Eq. (8). Hence, the interface of porous clear flow indeed is not a real boundary, and it is a part of the internal domain. At the initial time, the PCM is solid, and the temperature of the whole domain is T_c.

The interfacial energy balance (Stefan condition) is utilized to achieve the displacement of the phase change interface:

$$k_{m,l}\left.\frac{\partial T}{\partial x}\right|_l - k_{m,s}\left.\frac{\partial T}{\partial x}\right|_s = \rho\varepsilon u L_{fs} \tag{12a}$$

$$k_{m,l}\left.\frac{\partial T}{\partial y}\right|_l - k_{m,s}\left.\frac{\partial T}{\partial y}\right|_s = \rho\varepsilon v L_{fs} \tag{12b}$$

To better analyze the problem, Eqs. (1)–(12) are transferred to the X–Y non-dimensional coordinates by introducing dimensionless variables as follows:

$$(X,Y,D,S) = \frac{(x,y,d,s)}{L},\ \tau = \frac{t\alpha_l}{L^2},\ (U,V) = \frac{(u,v)L}{\alpha_l},\ P = \frac{pL^2}{\rho_l \alpha_l^2}$$
$$\theta = \frac{T - T_c}{T_h - T_c},\ Ra = \frac{g\beta\left(T_h - T_c\right)L^3}{\nu_l \alpha_l},\ Pr = \frac{\nu_l}{\alpha_l},\ Da = \frac{K}{L^2},\ Ste = \frac{C_{p,l}\left(T_h - T_c\right)}{L_{fs}} \tag{13}$$

Substituting Eq. (13) into Eqs. (1)–(12), the corresponding non-dimensional form of the governing Eqs. (14)–(25) is obtained as:

Continuity:

$$\frac{\partial U}{\partial X} + \frac{\partial V}{\partial Y} = 0 \tag{14}$$

Momentum in X-direction:

$$\frac{1}{\varepsilon}\frac{\partial U}{\partial \tau} + \frac{1}{\varepsilon^2}\left(U\frac{\partial U}{\partial X} + V\frac{\partial U}{\partial Y}\right) = -\frac{\partial P}{\partial X} + \frac{Pr}{\varepsilon}\left(\frac{\partial^2 U}{\partial X^2} + \frac{\partial^2 U}{\partial Y^2}\right) - \frac{Pr}{Da}U + PrRa\theta_l \sin(\gamma) \tag{15}$$

Momentum in Y-direction:

$$\frac{1}{\varepsilon}\frac{\partial V}{\partial \tau} + \frac{1}{\varepsilon^2}\left(U\frac{\partial V}{\partial X} + V\frac{\partial V}{\partial Y}\right) = -\frac{\partial P}{\partial Y} + \frac{Pr}{\varepsilon}\left(\frac{\partial^2 V}{\partial X^2} + \frac{\partial^2 V}{\partial Y^2}\right) - \frac{Pr}{Da}V + PrRa\theta_l \cos(\gamma) \tag{16}$$

where Ra the Rayleigh number, Pr the Prandtl number, Da the Darcy number, respectively, are:

$$Ra = \frac{g\beta\left(T_l - T_c\right)L^3}{\nu_l \alpha_l}, Pr = \frac{\nu_l}{\alpha_l}, Da = \frac{K}{L^2} \tag{17}$$

The Darcy number Da and porosity ε are introduced as a space-dependent function as:

$$Da = Da\ \text{step}(X) + \infty \times (1 - \text{step}(X)) \tag{18a}$$

$$\varepsilon = \varepsilon\ \text{step}(X) + (1 - \text{step}(X)) \tag{18b}$$

where the non-dimensional form of the step function step(X) is obtained as:

$$\text{step}(X) = \begin{cases} 1 & D < X < S \\ 0 & X > S \end{cases} \tag{19}$$

Energy balance for melted PCM:

$$\frac{(\rho C_p)_{m,l}}{(\rho C_p)_l}\left(\frac{\partial \theta_l}{\partial \tau}\right) + \left(U\frac{\partial \theta_l}{\partial X} + V\frac{\partial \theta_l}{\partial Y}\right) = \frac{k_{m,l}}{k_l}\left(\frac{\partial^2 \theta_l}{\partial X^2} + \frac{\partial^2 \theta_l}{\partial Y^2}\right) \tag{20}$$

Energy balance for solid PCM:

$$\frac{(\rho C_p)_{m,s}}{(\rho C_p)_l}\left(\frac{\partial \theta_s}{\partial \tau}\right) = \frac{k_{m,s}}{k_l}\left(\frac{\partial^2 \theta_s}{\partial X^2} + \frac{\partial^2 \theta_s}{\partial Y^2}\right) \tag{21}$$

Energy balance for the solid wall:

$$\frac{\left(\rho C_p\right)_w}{\left(\rho C_p\right)_l}\frac{\partial \theta_w}{\partial \tau} = \left(\frac{k_w}{k_l}\right)\left(\frac{\partial^2 \theta_w}{\partial X^2} + \frac{\partial^2 \theta_w}{\partial Y^2}\right) \tag{22}$$

The non-dimensional forms of the boundary conditions are:
On the wall–porous interface:

$$\begin{aligned} &\theta_w\big|_{wall} = \theta_l\big|_{porous} \\ &\frac{k_w}{k_l}\frac{\partial \theta_w}{\partial n}\bigg|_{wall} = \frac{k_{m,l}}{k_l}\frac{\partial \theta}{\partial n}\bigg|_{porous} \quad or \quad \frac{k_w}{k_l}\frac{\partial \theta_w}{\partial n}\bigg|_{wall} = \frac{k_{m,s}}{k_l}\frac{\partial \theta}{\partial n}\bigg|_{porous} \end{aligned} \tag{23}$$

On the external surfaces:

$$\begin{aligned} &\begin{cases} \theta_w(0,Y) = 1 & Z - B/2 \le Y \le Z + B/2 \\ \frac{\partial \theta_w(0,Y)}{\partial X} = 0 & Y \ge Z + B/2\ \&\ Y \le Z - B/2 \end{cases} \\ &U(1,Y) = V(1,Y) = 0, \quad \theta(1,Y) = 0 \\ &U(X,0) = V(X,0) = 0, \quad \frac{\partial \theta_w(X,0)}{\partial Y} = \frac{\partial \theta(X,0)}{\partial Y} = 0 \\ &U(X,1) = V(X,1) = 0, \quad \frac{\partial \theta_w(X,1)}{\partial Y} = \frac{\partial \theta(X,1)}{\partial Y} = 0 \end{aligned} \tag{24}$$

Considering the dimensionless temperature definition, the initial temperature is zero in the non-dimensional form. Non-dimensional displacement velocity of the moving melting interface in X- and Y-directions:

$$U = \frac{Ste}{\varepsilon}\left(\frac{k_{m,l}}{k_l}\frac{\partial\theta}{\partial X}\bigg|_l - \frac{k_{m,s}}{k_l}\frac{\partial\theta}{\partial X}\bigg|_s\right) \tag{25a}$$

$$V = \frac{Ste}{\varepsilon}\left(\frac{k_{m,l}}{k_l}\frac{\partial\theta}{\partial Y}\bigg|_l - \frac{k_{m,s}}{k_l}\frac{\partial\theta}{\partial Y}\bigg|_s\right) \tag{25b}$$

The non-dimensional thermophysical properties can be summarized as:

$$\begin{aligned}
\frac{k_{m,l}}{k_l} &= (1-\varepsilon)\frac{k_p}{k_l} + \varepsilon \\
\frac{k_{m,s}}{k_l} &= (1-\varepsilon)\frac{k_p}{k_l} + \varepsilon\frac{k_s}{k_l} \\
\frac{(\rho C_p)_{m,l}}{(\rho C_p)_l} &= (1-\varepsilon)\frac{(\rho C_p)_p}{(\rho C_p)_l} + \varepsilon \\
\frac{(\rho C_p)_{m,s}}{(\rho C_p)_l} &= (1-\varepsilon)\frac{(\rho C_p)_p}{(\rho C_p)_l} + \varepsilon\frac{(\rho C_p)_s}{(\rho C_p)_l}
\end{aligned} \tag{26}$$

where considering the thermophysical properties in Tables 1 and 2 the thermophysical ratios are fixed as $k_p/k_l = k_w/k_l = 1025$, $k_s/k_l = 1.15$, $(\rho C_p)_p/(\rho C_p)_l = (\rho C_p)_w/(\rho C_p)_l = 1.6243$, and $(\rho C_p)_s/(\rho C_p)_l = 1.1447$ in the present study.

It should be noted that the porosity is a function of X defined by Eq. (18b). In this study, the porosity value in the porous region is considered to be 0.92 [1]. The Nusselt at the heated wall and the volume fraction of melt are the parameters of interest. A part of the enclosures is filled with the porous matrix, and the PCM can only fill the void space in the pores and the porosity in the clear space is unit. Hence, the void space in the porous space and in the clear space which is filled with PCM can be evaluated using the porosity function. So, the melt volume fraction is presented as:

$$MVF = \int_0^1 \int_D^{X_m} \varepsilon \, dXdY \tag{27}$$

where MVF indicates the melt volume fraction of the melted PCM, and the m subscript represents the location of the solid–liquid interface. As the presence of the porous matrix reduces the void volume of the cavity, the normalized MVF (NMVF) can be introduced as the actual melt volume fraction compared to the void molten capacity of the cavity, including the porous media as:

$$NMVF = \frac{\int_0^1 \int_D^{X_m} \varepsilon \, dXdY}{\int_0^1 \int_D^1 \varepsilon \, dXdY} \tag{28}$$

The energy transfer at the heated wall is computed using the energy balance as:

$$q = -Ak_w \frac{\partial T_w}{\partial x}\Bigg)_{x=-d} \tag{29}$$

where using the non-dimensional parameters it can be written as:

$$Q_Y = -\frac{\partial \theta_w}{\partial X}\Bigg)_{X=0} \tag{30}$$

where $Q_Y = qL/k_w(T_h - T_c)$ is the non-dimensional heat transfer at the wall and the total heat transfer at the wall can be obtained by integration over the length of the wall as:

$$Q = \int_{Z-B/2}^{Z+B/2} Q_Y \mathrm{d}Y. \tag{31}$$

3 Numerical Method, Grid Test, and Validation

3.1 Numerical Method

The powerful numerical approach of the finite element was adopted to solve the set of Eqs. (14)–(16) and (20)–(22), subject to the boundary conditions with Eqs. (23) and (24). The details of the numerical approach are presented in (Basak et al. 2006; Reddy 1993). The numerical method uses the continuity equation and a penalty parameter (γ) for the coupling of the velocity and pressure (Reddy 1993).

$$P = -\gamma\left(\frac{\partial U}{\partial X} + \frac{\partial V}{\partial Y}\right) \tag{32}$$

$$\frac{1}{\varepsilon}\frac{\partial U}{\partial \tau} + \frac{1}{\varepsilon^2}\left(U\frac{\partial U}{\partial X} + V\frac{\partial V}{\partial Y}\right) = -\frac{\partial}{\partial X}\left[-\gamma\left(\frac{\partial U}{\partial X} + \frac{\partial V}{\partial Y}\right)\right] + \frac{Pr}{\varepsilon}\left(\frac{\partial^2 U}{\partial X^2} + \frac{\partial^2 U}{\partial Y^2}\right) - \frac{Pr}{Da}U + PrRa\theta_l \sin(\gamma) \tag{33}$$

$$\frac{1}{\varepsilon}\frac{\partial V}{\partial \tau} + \frac{1}{\varepsilon^2}\left(U\frac{\partial V}{\partial X} + V\frac{\partial V}{\partial Y}\right) = -\frac{\partial}{\partial Y}\left[-\gamma\left(\frac{\partial U}{\partial X} + \frac{\partial V}{\partial Y}\right)\right] + \frac{Pr}{\varepsilon}\left(\frac{\partial^2 V}{\partial X^2} + \frac{\partial^2 V}{\partial Y^2}\right) - \frac{Pr}{Da}V + PrRa\theta_l \cos(\gamma) \tag{34}$$

It is evident that very large values of the penalty parameter ($\gamma = 10^7$) can satisfy the continuity Equation [5]. Now, the velocities components (i.e., U and V), and temperatures are expanded invoking a basis set $\{\zeta_k\}_{k=1}^N$ as,

$$\begin{aligned} U &\approx \sum_{k=1}^{N} (U)_k \zeta_k(X,Y), V \approx \sum_{k=1}^{N} (V)_k \zeta_k(X,Y), \theta_l \approx \sum_{k=1}^{N} \theta_{l,k}\zeta_k(X,Y) \\ \theta_s &\approx \sum_{k=1}^{N} \theta_{s,k}\zeta_k(X,Y), \theta_w \approx \sum_{k=1}^{N} \theta_{w,k}\zeta_k(X,Y) \end{aligned} \tag{35}$$

In the domain of the solution. Since the basis functions for the velocity components and the temperatures are the same, the total number of nodes variables is N. The nonlinear residuals for the discussed equations at nodes of internal domain Ω are derived as,

$$\begin{aligned} R_i^{(1)} = & \sum_{k=1}^{N} \frac{U_k}{\varepsilon} \int_{\Omega} \frac{\partial \zeta_k}{\partial \tau} dXdY + \sum_{k=1}^{N} \frac{U_k}{\varepsilon^2} \int_{\Omega} \left[\left(\sum_{k=1}^{N} U_k \zeta_k \right) \frac{\partial \zeta_k}{\partial X} + \left(\sum_{k=1}^{N} V_k \zeta_k \right) \frac{\partial \zeta_k}{\partial Y} \right] \zeta_i dXdY \\ & + \frac{Pr}{\varepsilon} \sum_{k=1}^{N} U_k \int_{\Omega} \left[\frac{\partial \zeta_i}{\partial X} \frac{\partial \zeta_k}{\partial X} + \frac{\partial \zeta_i}{\partial Y} \frac{\partial \zeta_k}{\partial Y} \right] dXdY - \frac{Pr}{Da} \sum_{k=1}^{N} \int_{\Omega} \left(\sum_{k=1}^{N} \left(U_k \zeta_k \right) \zeta_i \right) dXdY \\ & + \chi \left[\sum_{k=1}^{N} U_k \int_{\Omega} \frac{\partial \zeta_i}{\partial X} \frac{\partial \zeta_k}{\partial X} dXdY + \sum_{k=1}^{N} V_k \int_{\Omega} \frac{\partial \zeta_i}{\partial X} \frac{\partial \zeta_k}{\partial Y} dXdY \right] \\ & + RaPr \left[\int_{\Omega} \left(\sum_{k=1}^{N} \theta_{l,k} \zeta_k \right) \zeta_i dXdY \right] \sin(\gamma) \end{aligned} \tag{36}$$

$$\begin{aligned} R_i^{(2)} = & \sum_{k=1}^{N} \frac{V_k}{\varepsilon} \int_{\Omega} \frac{\partial \zeta_k}{\partial \tau} dXdY + \sum_{k=1}^{N} \frac{V_k}{\varepsilon^2} \int_{\Omega} \left[\left(\sum_{k=1}^{N} U_k \zeta_k \right) \frac{\partial \zeta_k}{\partial X} + \left(\sum_{k=1}^{N} V_k \zeta_k \right) \frac{\partial \zeta_k}{\partial Y} \right] \zeta_i dXdY \\ & + \frac{Pr}{\varepsilon} \sum_{k=1}^{N} V_k \int_{\Omega} \left[\frac{\partial \zeta_i}{\partial X} \frac{\partial \zeta_k}{\partial X} + \frac{\partial \zeta_i}{\partial Y} \frac{\partial \zeta_k}{\partial Y} \right] dXdY - \frac{Pr}{Da} \sum_{k=1}^{N} \int_{\Omega} \left(\sum_{k=1}^{N} \left(V_k \zeta_k \right) \zeta_i \right) dXdY \\ & + \chi \left[\sum_{k=1}^{N} U_k \int_{\Omega} \frac{\partial \zeta_i}{\partial Y} \frac{\partial \zeta_k}{\partial X} dXdY + \sum_{k=1}^{N} V_k \int_{\Omega} \frac{\partial \zeta_i}{\partial Y} \frac{\partial \zeta_k}{\partial Y} dXdY \right] \\ & + RaPr \left[\int_{\Omega} \left(\sum_{k=1}^{N} \theta_{l,k} \zeta_k \right) \zeta_i dXdY \right] \cos(\gamma) \end{aligned} \tag{37}$$

$$\begin{aligned} R_i^{(3)} = & + \sum_{k=1}^{N} \theta_{l,k} \int_{\Omega} \left[\sum_{k=1}^{N} \left(U_k \zeta_k \right) \frac{\partial \zeta_k}{\partial X} + \sum_{k=1}^{N} \left(V_k \zeta_k \right) \frac{\partial \zeta_k}{\partial Y} \right] \zeta_i dXdY \\ & + \frac{k_{m,l}}{k_l} \left(\sum_{k=1}^{N} \theta_{l,k} \int_{\Omega} \left[\frac{\partial \zeta_i}{\partial X} \frac{\partial \zeta_k}{\partial X} + \frac{\partial \zeta_i}{\partial Y} \frac{\partial \zeta_k}{\partial Y} \right] dXdY \right) \\ & \times \frac{(\rho C_p)_{m,l}}{(\rho C_p)_l} \left(\sum_{k=1}^{N} \theta_{l,k} \int_{\Omega} \frac{\partial \zeta_k}{\partial \tau} \zeta_i dXdY \right) \end{aligned} \tag{38}$$

$$R_i^{(4)} = \frac{(\rho C_p)_{m,s}}{(\rho C_p)_l} \left(\sum_{k=1}^{N} \theta_{s,k} \int_{\Omega} \frac{\partial \zeta_k}{\partial \tau} \zeta_i dXdY \right) + \frac{k_{m,s}}{k_l} \left(\sum_{k=1}^{N} \theta_{s,k} \int_{\Omega} \left[\frac{\partial \zeta_i}{\partial X} \frac{\partial \zeta_k}{\partial X} + \frac{\partial \zeta_i}{\partial Y} \frac{\partial \zeta_k}{\partial Y} \right] dXdY \right) \tag{39}$$

$$R_i^{(5)} = \frac{\left(\rho C_p\right)_w}{\left(\rho C_p\right)_l}\left(\sum_{k=1}^{N}\theta_{w,k}\int_{\Omega}\frac{\partial\zeta_k}{\partial\tau}\zeta_i dXdY\right) + \frac{k_w}{k_l}\left(\sum_{k=1}^{N}\theta_{w,k}\int_{\Omega}\left[\frac{\partial\zeta_i}{\partial X}\frac{\partial\zeta_k}{\partial X}+\frac{\partial\zeta_i}{\partial Y}\frac{\partial\zeta_k}{\partial Y}\right]dXdY\right) \tag{40}$$

A reference pressure at the top of the wall–fluid interface with zero pressure was introduced. Moreover, some constraints were introduced to limit the vertical grid motion next to the horizontal bounds, preventing inverted low-quality grids. In this case, the vertical grid movement was converted to the same horizontal grid movement to produce the same amount of liquid fraction. The grid motion was also controlled very close to the cold wall preventing the grid collision with the cold wall. When the grid reaches to $X=1$, the grid motion stops. It should be noted the length of the cavity was considered as $X=1.1$ due to mesh control. However, the computations were performed in the cavity of non-dimensional size $X=Y=1$, and the region between $X=1$ and $X=1.1$ was discarded in any characteristic calculation.

The results were recorded at the strict time steps of $\Delta\tau=5\times10^{-4}$. However, an automatic time step scheme based on the backward differentiation formulas (BDF) with embedded error control was utilized for controlling the intermediate time steps. Here, the automatic time step scheme ensures the accuracy of the solution. BDF employs a numerical estimate of the local truncation error along with a time step selector (Moore and Petzold 1994) to control the time steps and maintain the solution within a given tolerance. The following relation evaluates the validity of each time step for the scaled absolute tolerance:

$$\left(\frac{1}{M}\sum_j\frac{1}{N_j}\sum_i\left(\frac{\left|E_{Y_i}\right|}{A_{s,i}+R\left|Y_i\right|}\right)^2\right)^{\frac{1}{2}} < 1 \tag{41}$$

where E_Y denotes the estimate of the local error (absolute error) in scaled solution vector (Y_i) and $A_{s,\,i}$ indicates the scaled absolute tolerance for degrees of freedom i. In the above equation, R, N_j, and M are the relative tolerance, number of degrees of freedom in field j, and number of fields, respectively.

3.2 Grid Test

The shape of the solid wall is a rectangle with no deformation. A structured grid was selected for this region. The PCM-filled solid and liquid regions were meshed using triangular elements. The triangular grids were easier to handle in the Arbitrary Eulerian–Lagrangian (ALE) domain. As there are three main domains of solid wall (domain A), solid region (domain B), and liquid region (domain C) with different physics, a systematic grid check was performed. A non-uniformed structured $N_x\times N_y$ mesh was used for domain A, i.e., the solid wall. In domain A, the grid points were uniform in the vertical direction (y), while the grids were stretched in the x-direction with the growth ratio of 0.1, in a way that the grids were fine next to the hot element.

A triangular mesh with the maximum size of MaxB was adopted for domain B. We presumed that the grid size in domain B, i.e., the solid region, was not important as there were no evident temperature gradients in this region. In contrast, the grid size in the liquid region was very important due to the temperature and velocity gradients. Hence, a fine

triangular mesh with the maximum size of MaxC was selected for domain C. The phase change interface was divided into N_y equal grid points the same as the size of domain A. For all triangular grids, the maximum element growth rate and curvature factor were 1.25 and 0.25, respectively.

First, a very fine grid was selected for domains A and B to diminish the effect of these regions on the solution, and then, the impact of the grid size of domain C, i.e., the liquid region, on the solution was investigated. Then, for a very fine and adequate mesh in domain C, the size of the mesh in domains A and B was increased. The governing equations were solved for various grid sizes. The distortion of the grids in the solid and liquid PCM regions was monitored. For any distortion larger than unity, a re-meshing was performed. Due to the growth of the liquid region and shrinkage of the solid region, the re-meshing was essential because of the melting phase change. The re-meshing ensures the quality of the grid during the large deformations of the liquid and solid domains.

For grid check, the governing equations were solved, and the heat transfer from the hot element, Q, was monitored and plotted as a function of the non-dimensional time. To explore the effect of the grid size on the accuracy of the results, each time, the grid size of a region was changed, while the other regions were kept at the smallest grid size to diminish their effects of the solution accuracy.

The size of the grid at the wall–fluid region and the melting interface (N_y) was shared between the domains. Moreover, the temperature and velocity gradients are significant next to these two surfaces. Hence, our preliminary results showed that N_y was the most important parameter of the grid in this study. The heat transfer results for three different grid sizes are plotted in Fig. 2. The selected parameters for the grid examination were $Pr=41.2$, $Ra=1.4\times10^7$, $Ste=0.11$, $Da=3.1\times10^{-4}$, $B=0.2$, $S=0.1$, $D=0.01$, and $\gamma=45°$. The details of the corresponding grids are summarized in Table 3. As shown in Fig. 2, the difference between the results is in the initial times. The grid of case 3 shows acceptable results with a reasonable computational cost. Hence, the grid of case 4 was utilized for plotting the results. Figure 3 shows the grid of case 4 at $\tau=0.1$. Figure 3b shows a detailed view of the grid at the top of the cavity.

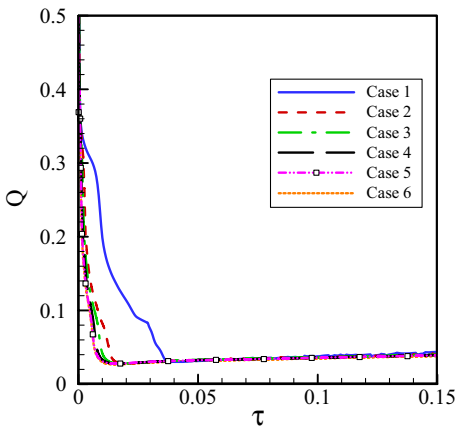

Fig. 2 Time history of the element heat flux (Q) for various grid sizes

Table 3 Details of each grid of case

Details	Case					
	1	2	3	4	5	6
Size A (N_x, N_y)	5×80	10×120	8×150	16×200	32×300	50×500
MaxB	0.07	0.06	0.05	0.04	0.03	0.02
MaxC	0.045	0.035	0.025	0.02	0.015	0.01
Element growth rate	1.25	1.25	1.25	1.25	1.25	1.25
Computational time	16 min	27 min	39 min	47 min	1 h 18 min	2 h 34 min
Number of elements	1631	4153	5374	9567	2106	48,194

3.3 Validation and Verification

The correctness and accuracy of the provided code were evaluated by comparing the results of this work and those mentioned in (Kashani et al. 2012; Bertrand et al. 1999; Gau and Viskanta 1986; Sun and Pop 2011; Sheremet et al. 2015; Sathiyamoorthy and Chamkha 2012). Figures 4, 5 and 6, and Table 4 show these verifications and validations. The results exhibit

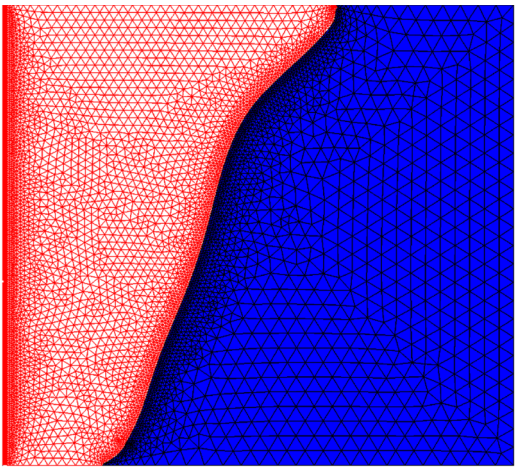

(a) Full view

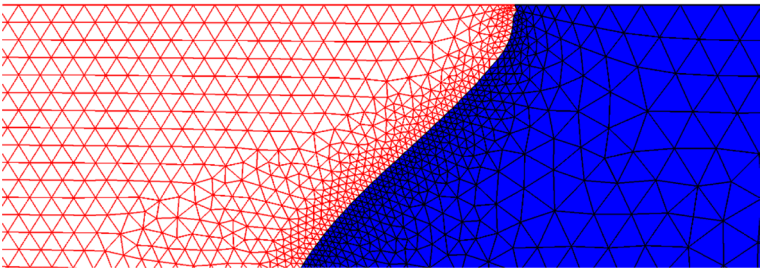

(b) Top view

Fig. 3 Grid of case 4 at $\tau = 0.1$, **a** Full view and **b** Top view

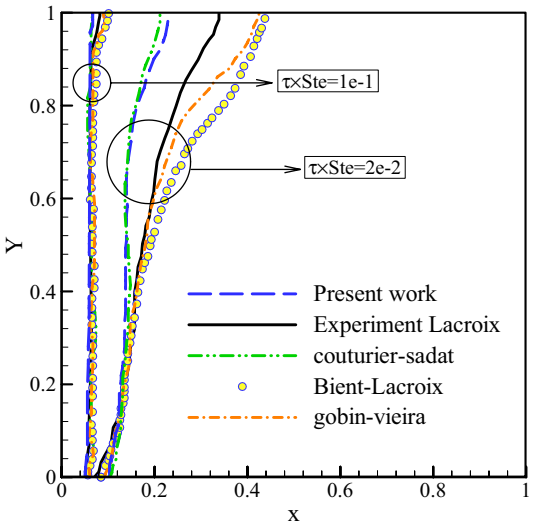

Fig. 4 Obtained melting interface of the current work and those of Bertrand et al. (1999)

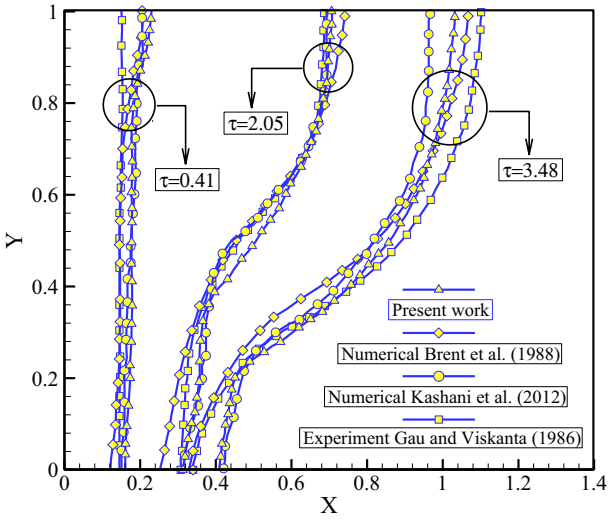

Fig. 5 Obtained melting interface of the current work and the literature (Gau and Viskanta 1986)

an acceptable agreement between the current simulations and the previous works. The leading cause of discrepancies between the results of numerical methods in Figs. 4 and 5 can be seen in the different approaches of capturing the melting interface, especially at the early stage of the phase change. Moreover, there are also different measuring techniques, which have been utilized in the literature. For instance, Gau and Viskanta (1986) utilized a mechanical probe to capture the melting interface.

4 Results and Discussion

4.1 Grid Deformation

Figure 7 shows the grid deformation during the melting process of PCM inside the cavity at different dimensionless times when $Pr=41.2$, $Ra=1.41\times10^{7}$, $Da=3.1\times10^{-4}$, $\gamma=0°$, $S=0.1$, and $Ste=0.11$. At the primary times, the melting process of the solid region is more significant at where the embedded heater is located on the left wall, so it leads to a convex shape of grid deformation. It is worth mentioning that the conduction heat transfer is dominant at this time, and gradually, the convection mechanism becomes predominant. Due to natural convection impacts, the mesh deformation approaches toward the upper parts of the cavity by the advancement of the melting process, and the melting process intensifies at top regions of the cavity. At the latest times of the melting process within the clear region, the convection heat transfer is the predominant mechanism, so the melted region covers the upper parts of the cavity sooner.

4.2 Analysis of the Effect of the Porous Layer Thickness

Figure 8 depicts the isotherms and streamlines of melted PCM for different porous layer thicknesses at $\tau=0.3$ when $D=0.001$, $Pr=41.2$, $Ra=1.41\times10^{7}$, $Da=3.1\times10^{-4}$, $Ste=0.11$, $\varepsilon=0.92$, and $\gamma=0°$. It can be seen that an increase in the porous layer thickness

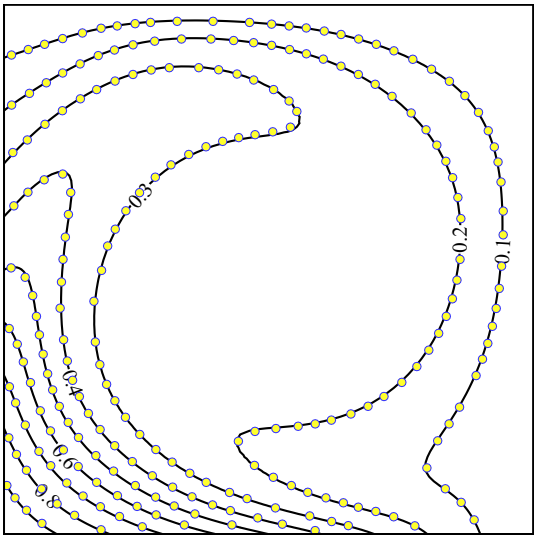

Fig. 6 Obtained isotherms of the current work (solid lines) and those of Sathiyamoorthy and Chamkha (2012) (points)

Table 4 Average Nusselt number in a porous triangular enclosure

$Ra\times Da$	Sun and Pop (2011)	Sheremet et al. (2015)	Present work
500	9.66	9.65	9.64
1000	13.9	14.05	13.96

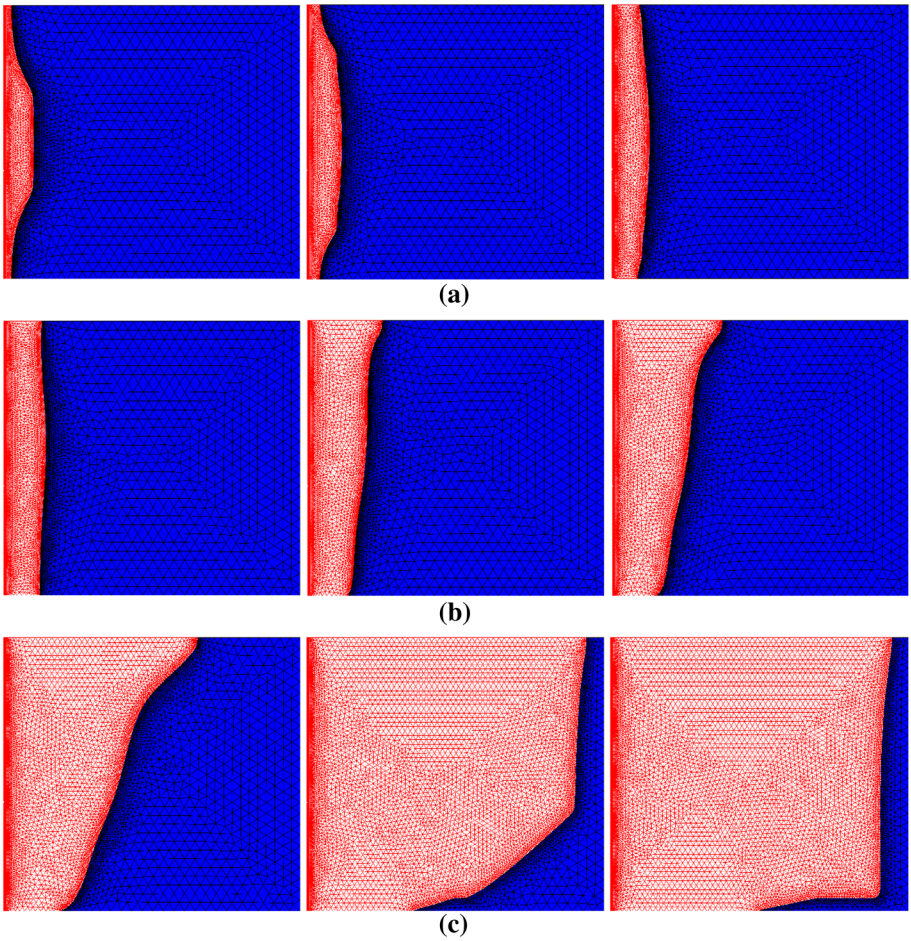

Fig. 7 Display of the deformable mesh during heat transfer process when $\gamma = 0°$, $D = 0.01$, and $S = 0.1$ for **a** $\tau = 0.001$, 0.003, and 0.005, **b** $\tau = 0.01$, 0.03, and 0.05, **c** $\tau = 0.1$, 0.3, and 0.5 (left to right)

leads to an increment in the melting area at similar *Fo* numbers. In thicker porous layers, there would be more effective thermal conductivity and uniform temperature distribution of the element, so the heat transfer rate, and hence, the melting rate is higher compared with the thinner layers. Figure 9 illustrates the effects of different porous layer thickness on the NMVF and the heat transfer rate for this case. It is evident that the melt volume fraction reaches its maximum, i.e., NMVF = 1, sooner (around $\tau = 0.12$) by thicker porous layer $S = 1$, while it is lower for other thicknesses. Also, the increase in porous layer thickness has a direct relation with an increment of heat transfer rate. It is the result of an empowered conduction heat transfer mechanism due to the porous media.

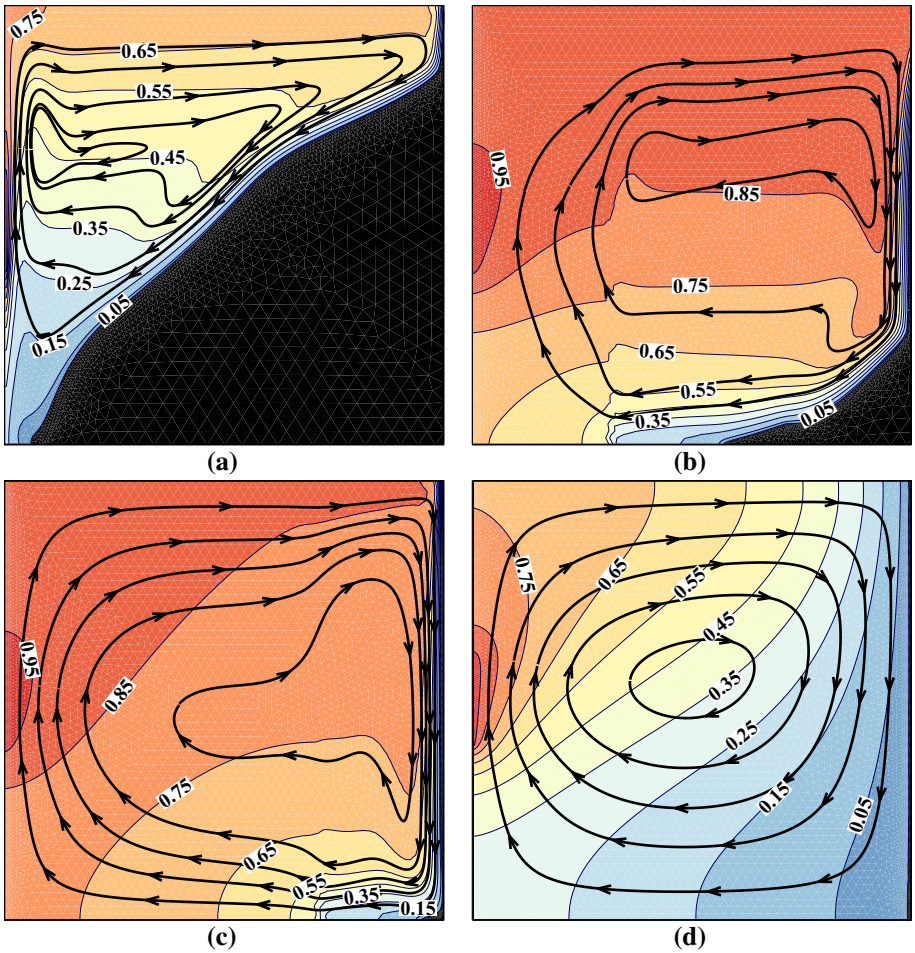

Fig. 8 Isotherms and streamlines for **a** $S=0.0$, **b** $S=0.3$, **c**: $S=0.7$, and **d** $S=1.0$ at $\tau=0.3$ when $D=0.001$, $Pr=41.2$, $Ra=1.41\times107$, $Da=3.1\times10^{-4}$, $Ste=0.11$, $\varepsilon=0.92$, and $\gamma=0°$

4.3 Analysis of the Effect of the Inclination Angle

Figure 10 shows the impacts of the inclination of the cavity on the isotherms and streamline of the melting process when $D=0.001$, $Pr=41.2$, $Ra=1.41\times10^{7}$, $Da=3.1\times10^{-4}$, $Ste=0.11$, and $\varepsilon=0.92$. Three various inclination angles ($\gamma=0°$, $\gamma=45°$, and $\gamma=90°$) have been surveyed in this research. It is evident that the inclination of the enclosure affects the melting area and the movement of the melting front. This is due to the changing of the buoyancy force distribution significantly while changing the cavity angle. Conduction heat transfer next to the hot wall in the solid region as well as the convection heat transfer at the porous and free layer leads to a convex form of melting at the cavity with $\gamma=90°$. Also, two separate regions for the streamlines are formed in $\gamma=90°$.

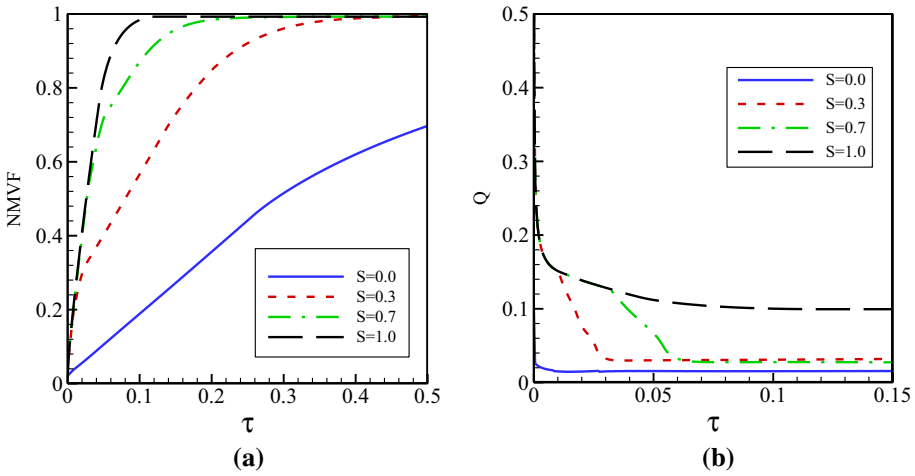

Fig. 9 Effect of S on **a** the NMVF and **b** the heat transfer rate when $D=0.001$, $Pr=41.2$, $Ra=1.41\times107$, $Da=3.1\times10^{-4}$, $Ste=0.11$, $\varepsilon=0.92$, and $\gamma=0°$

Figure 11 illustrates the effect of the inclination angle, i.e., γ, on the NMWF and the heat transfer rate. An ascending and descending trend can be seen for NMWF and the heat transfer rate by the time, respectively. The NMVF of the inclined cavity is higher than the horizontal one, especially for $\gamma=45°$. The heat transfer rate shows a sharp fall at primary times ($\tau<0.01$). At the beginning of the melting process, the extreme gradient of the temperature between the hot wall and the PCM causes a dramatic rate of the conductive heat transfer, and gradually, the temperature gradient diminishes by the advancement of melting front, and hence, the heat transfer rate decreases.

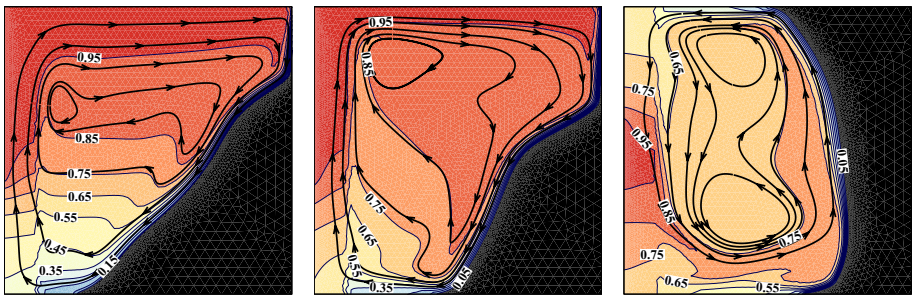

Fig. 10 Isotherms and streamlines for **a** $\gamma=0°$, **b** $\gamma=45°$, and **c** $\gamma=90°$ at $\tau=0.2$ when $S=0.1$, $Pr=41.2$, $Ra=1.41\times107$, $Da=3.1\times10^{-4}$, $Ste=0.11$, $\varepsilon=0.92$, and $D=0.001$

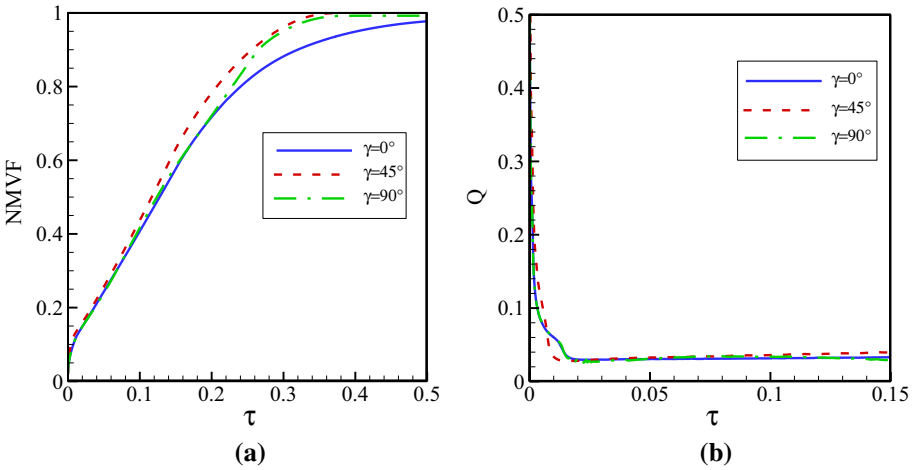

Fig. 11 Effect of the inclination angle γ on **a** the NMWF and **b** the heat transfer rate when $D=0.001$, $S=0.1$, $Pr=41.2$, $Ra=1.41\times107$, $Da=3.1\times10^{-4}$, $Ste=0.11$, and $\varepsilon=0.92$

4.4 Analysis of the Effect of the Wall Thickness (D)

Figures 12 and 13 illustrate the impact of the wall thickness on the melting process, normalized melted volume fraction, and the heat transfer rate at $\tau=0.1$ when $Pr=41.2$, $Ra=1.41\times10^{7}$, $Da=3.1\times10^{-4}$, $Ste=0.11$, $\varepsilon=0.92$, $S=0.1$, and $\gamma=0°$. As shown, the temperature field becomes more uniform as the wall thickness increases. When the wall is thin, the heat is locally transferred to the PCM where the heater is located. However, the presence of the thick wall causes the heat to uniformly transfer to the PCM through the interface of the solid wall and PCM. At primary times, the conduction mechanism is predominant, the ticker walls conduct more heat into the cavity. After that, the convection heat transfer gradually becomes dominant, and hence, the impact of the wall thickens on the overall heat transfer declines. Also, it can be found that the melting rate increases with an increase in wall thickness.

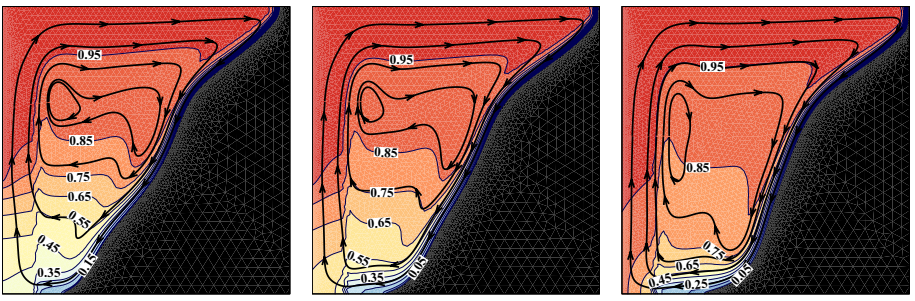

Fig. 12 Isotherms and Stream Line for **a** $D=0.001$, **b** $D=0.01$, and **c** $D=0.1$ at $\tau=0.15$ when $Pr=41.2$, $Ra=1.41\times107$, $Da=3.1\times10^{-4}$, $Ste=0.11$, $\varepsilon=0.92$, $S=0.1$, and $\gamma=0°$

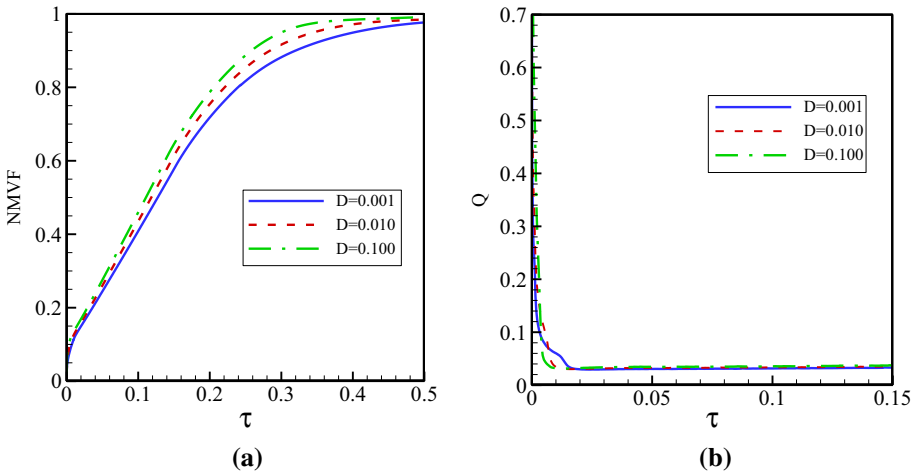

Fig. 13 Effect of the wall thickness D on **a** the NMVF and **b** the heat transfer rate when $Pr=41.2$, $Ra=1.41\times107$, $Da=3.1\times10^{-4}$, $Ste=0.11$, $\varepsilon=0.92$, $S=0.1$, and $\gamma=0°$

5 Conclusion

The melting flow and heat transfer in an inclined compound cavity, including a solid wall, porous layer, and clear region are addressed in this study. The width of the porous layer and the clear region is fixed, and a hot element is placed at the left side of the porous layer. To track the interface of the melted liquid and solid regions, the Stefan condition is applied. The finite element method, along with the ALE moving grid technique, is employed to solve the non-dimensional governing equations. The grid check is conducted, and the outcomes in several cases are validated against the available literature. The effect of the wall thickness, the porous layer thickness, and the inclination angle of the cavity on the melting process of PCMs is investigated. It is found that the porous layer thickness drastically affects the melting process and heat transfer rate. The melting and heat transfer rates are increased by increasing the thickness of the porous layer. Also, it is found that the melting rate is higher when the inclination angle is 45°. Increasing the wall thickness leads to an augmentation in the melting rate.

References

Al-Jethelah, M.S., Tasnim, S.H., Mahmud, S., Dutta, A.: Melting of nano-phase change material inside a porous enclosure. Int. J. Heat Mass Transf. **102**, 773–787 (2016)

Alsabery, A., Ismael, M., Chamkha, A., Hashim, I.: Numerical investigation of mixed convection and entropy generation in a wavy-walled cavity filled with nanofluid and involving a rotating cylinder. Entropy **20**, 664 (2018a)

Alsabery, A., Sheremet, M., Chamkha, A., Hashim, I.: Conjugate natural convection of Al2O3–water nanofluid in a square cavity with a concentric solid insert using Buongiorno's two-phase model. Int. J. Mech. Sci. **136**, 200–219 (2018b)

Alsabery, A., Sheremet, M., Chamkha, A., Hashim, I.: MHD convective heat transfer in a discretely heated square cavity with conductive inner block using two-phase nanofluid model. Sci. Rep. **8**, 7410 (2018c)

Alsabery, A., Ismael, M., Chamkha, A., Hashim, I.: Effects of two-phase nanofluid model on MHD mixed convection in a lid-driven cavity in the presence of conductive inner block and corner heater. J. Therm. Anal. Calorim. **135**, 729–750 (2019a)

Alsabery, A., Sheremet, M.A., Chamkha, A., Hashim, I.: Impact of nonhomogeneous nanofluid model on transient mixed convection in a double lid-driven wavy cavity involving solid circular cylinder. Int. J. Mech. Sci. **150**, 637–655 (2019b)

Alsabery, A.I., Mohebbi, R., Chamkha, A.J., Hashim, I.: Effect of local thermal non-equilibrium model on natural convection in a nanofluid-filled wavy-walled porous cavity containing inner solid cylinder. Chem. Eng. Sci. **201**, 247–263 (2019c)

Basak, T., Roy, S., Paul, T., Pop, I.: Natural convection in a square cavity filled with a porous medium: effects of various thermal boundary conditions. Int. J. Heat Mass Transf. **49**, 1430–1441 (2006)

Bechiri, M., Mansouri, K.: Study of heat and fluid flow during melting of PCM inside vertical cylindrical tube. Int. J. Therm. Sci. **135**, 235–246 (2019)

Bertrand, O., Binet, B., Combeau, H., Couturier, S., Delannoy, Y., Gobin, D., Lacroix, M., Le Quéré, P., Médale, M., Mencinger, J.: Melting driven by natural convection a comparison exercise: first results. Int. J. Therm. Sci. **38**, 5–26 (1999)

Bondareva, N., Sheremet, M.: Numerical investigation of the two-dimensional natural convection inside the system based on phase change material with a source of volumetric heat generation. Thermophys. Aeromech. **25**, 525–537 (2018)

Bondareva, N.S., Buonomo, B., Manca, O., Sheremet, M.A.: Heat transfer performance of the finned nano-enhanced phase change material system under the inclination influence. Int. J. Heat Mass Transf. **135**, 1063–1072 (2019)

Buongiorno, J.: Convective transport in nanofluids. J. Heat Transf. **128**, 240–250 (2006)

Chamkha, A., Doostanidezfuli, A., Izadpanahi, E., Ghalambaz, M.: Phase-change heat transfer of single/hybrid nanoparticles-enhanced phase-change materials over a heated horizontal cylinder confined in a square cavity. Adv. Powder Technol. **28**, 385–397 (2017)

Chamkha, A., Selimefendigil, F.: MHD free convection and entropy generation in a corrugated cavity filled with a porous medium saturated with nanofluids. Entropy **20**, 846 (2018)

Dinesh, B.V.S., Bhattacharya, A.: Effect of foam geometry on heat absorption characteristics of PCM-metal foam composite thermal energy storage systems. Int. J. Heat Mass Transf. **134**, 866–883 (2019)

Doostani, A., Ghalambaz, M., Chamkha, A.J.: MHD natural convection phase-change heat transfer in a cavity: analysis of the magnetic field effect. J. Braz. Soc. Mech. Sci. Eng. **39**, 2831–2846 (2017)

Elsayed, A.O.: Numerical investigation on PCM melting in triangular cylinders. Alex. Eng. J. **57**, 2819–2828 (2018)

Faghani, M., Hosseini, M.J., Bahrampoury, R.: Numerical simulation of melting between two elliptical cylinders. Alex. Eng. J. **57**, 577–586 (2018)

Fan, L., Khodadadi, J.M.: Thermal conductivity enhancement of phase change materials for thermal energy storage: a review. Renew. Sustain. Energy Rev. **15**, 24–46 (2011)

Farid, M.M., Khudhair, A.M., Razack, S.A.K., Al-Hallaj, S.: A review on phase change energy storage: materials and applications. Energy Convers. Manage. **45**, 1597–1615 (2004)

Gau, C., Viskanta, R.: Melting and solidification of a pure metal on a vertical wall. J. Heat Transf. **108**, 174–181 (1986)

Ghalambaz, M., Sabour, M., Pop, I.: Free convection in a square cavity filled by a porous medium saturated by a nanofluid: viscous dissipation and radiation effects. Eng. Sci. Technol. Int. J. **19**, 1244–1253 (2016)

Ghalambaz, M., Doostani, A., Izadpanahi, E., Chamkha, A.: Phase-change heat transfer in a cavity heated from below: the effect of utilizing single or hybrid nanoparticles as additives. J. Taiwan Inst. Chem. Eng. **72**, 104–115 (2017a)

Ghalambaz, M., Doostanidezfuli, A., Zargartalebi, H., Chamkha, A.J.: MHD phase change heat transfer in an inclined enclosure: effect of a magnetic field and cavity inclination. Numer. Heat Transf. Part A Appl. **71**, 91–109 (2017b)

Hayat, T., Khan, M.I., Waqas, M., Alsaedi, A., Farooq, M.: Numerical simulation for melting heat transfer and radiation effects in stagnation point flow of carbon–water nanofluid. Comput. Methods Appl. Mech. Eng. **315**, 1011–1024 (2017)

Hlimi, M., Hamdaoui, S., Mahdaoui, M., Kousksou, T., Ait Msaad, A., Jamil, A.E., Bouardi, A.: Melting inside a horizontal cylindrical capsule. Case Stud. Therm. Eng. **8**, 359–369 (2016)

Hu, J.-T., Mei, S.-J., Liu, D., Zhao, F.-Y., Wang, H.-Q.: Buoyancy driven double diffusive moisture convection inside the fluid-porous-solid sandwiched building enclosure containing internal heating sources. Int. J. Heat Mass Transf. **123**, 600–615 (2018)

Ismael, M.A.: Double-diffusive mixed convection in a composite porous enclosure with arc-shaped moving wall: tortuosity effect. J. Porous Med. **21**(4), 343–362 (2018)
Ismael, M.A., Ghalib, H.S.: Double diffusive natural convection in a partially layered cavity with inner solid conductive body. Sci Iran **25**, 2643–2659 (2018)
Jourabian, M., Darzi, A.A.R., Toghraie, D., Akbari, O.A.: Melting process in porous media around two hot cylinders: Numerical study using the lattice Boltzmann method. Phys. A **509**, 316–335 (2018a)
Jourabian, M., Farhadi, M.R., Darzi, A.: Constrained ice melting around one cylinder in horizontal cavity accelerated using three heat transfer enhancement techniques. Int. J. Therm. Sci. **125**, 231–247 (2018b)
Kashani, S., Ranjbar, A., Abdollahzadeh, M., Sebti, S.: Solidification of nano-enhanced phase change material (NEPCM) in a wavy cavity. Heat Mass Transf. **48**, 1155–1166 (2012)
Khodadadi, J., Hosseinizadeh, S.: Nanoparticle-enhanced phase change materials (NEPCM) with great potential for improved thermal energy storage. Int. Commun. Heat Mass Transf. **34**, 534–543 (2007)
Kumar, L., Manjunath, B., Patel, R., Markandeya, S., Agrawal, R., Agrawal, A., Kashyap, Y., Sarkar, P., Sinha, A., Iyer, K.: Experimental investigations on melting of lead in a cuboid with constant heat flux boundary condition using thermal neutron radiography. Int. J. Therm. Sci. **61**, 15–27 (2012)
Mehryan, S., Ghalambaz, M., Izadi, M.: Conjugate natural convection of nanofluids inside an enclosure filled by three layers of solid, porous medium and free nanofluid using Buongiorno's and local thermal non-equilibrium models. J. Therm. Anal. Calorim. **135**, 1047–1067 (2019a)
Mehryan, S., Izadi, M., Namazian, Z., Chamkha, A.J.: Natural convection of multi-walled carbon nanotube–Fe 3 O 4/water magnetic hybrid nanofluid flowing in porous medium considering the impacts of magnetic field-dependent viscosity. J. Therm. Anal. Calorim. **138**, 1541–1555 (2019b)
Moore, P.K., Petzold, L.R.: A stepsize control strategy for stiff systems of ordinary differential equations. Appl. Numer. Math. **15**, 449–463 (1994)
Nield, D.A., Bejan, A.: Convection in Porous Media. Springer, Berlin (2006)
Pop, I., Ghalambaz, M., Sheremet, M.: Free convection in a square porous cavity filled with a nanofluid using thermal non equilibrium and Buongiorno models. Int. J. Numer. Meth. Heat Fluid Flow **26**, 671–693 (2016)
Rakotondrandisa, A., Danaila, I., Danaila, L.: Numerical modelling of a melting-solidification cycle of a phase-change material with complete or partial melting. Int. J. Heat Fluid Flow **76**, 57–71 (2019)
Reddy, J.N.: An Introduction to the Finite Element Method. McGraw-Hill, New York (1993An)
Sathiyamoorthy, M., Chamkha, A.J.: Natural convection flow under magnetic field in a square cavity for uniformly (or) linearly heated adjacent walls. Int. J. Numer. Methods Heat Fluid Flow **22**(5), 677–698 (2012)
Sheikholeslami, M.: Numerical mosdeling of nano enhanced PCM solidification in an enclosure with metallic fin. J. Mol. Liq. **259**, 424–438 (2018a)
Sheikholeslami, M.: Numerical simulation for solidification in a LHTESS by means of Nano-enhanced PCM. J. Taiwan Inst. Chem. Eng. **86**, 25–41 (2018b)
Sheikholeslami, M.: Solidification of NEPCM under the effect of magnetic field in a porous thermal energy storage enclosure using CuO nanoparticles. J. Mol. Liq. **263**, 303–315 (2018c)
Sheikholeslami, M.: New computational approach for exergy and entropy analysis of nanofluid under the impact of Lorentz force through a porous media. Comput. Methods Appl. Mech. Eng. **344**, 319–333 (2019a)
Sheikholeslami, M.: Numerical approach for MHD Al2O3-water nanofluid transportation inside a permeable medium using innovative computer method. Comput. Methods Appl. Mech. Eng. **344**, 306–318 (2019b)
Sheikholeslami, M., Haq, R.-U., Shafee, A., Li, Z.: Heat transfer behavior of nanoparticle enhanced PCM solidification through an enclosure with *V* shaped fins. Int. J. Heat Mass Transf. **130**, 1322–1342 (2019a)
Sheikholeslami, M., Saleem, S., Shafee, A., Li, Z., Hayat, T., Alsaedi, A., Khan, M.I.: Mesoscopic investigation for alumina nanofluid heat transfer in permeable medium influenced by Lorentz forces. Comput. Methods Appl. Mech. Eng. **349**, 839–858 (2019b)
Sheikholeslami, M., Shamlooei, M., Moradi, R.: Fe3O4-Ethylene glycol nanofluid forced convection inside a porous enclosure in existence of coulomb force. J. Mol. Liq. **249**, 429–437 (2018)
Sheremet, M.A., Grosan, T., Pop, I.: Free convection in a square cavity filled with a porous medium saturated by nanofluid using Tiwari and Das' nanofluid model. Transp. Porous Media **106**, 595–610 (2015)
Sheremet, M.A., Pop, I., Baytas, A.C.: Non-equilibrium natural convection in a differentially-heated nanofluid cavity partially filled with a porous medium. Int. J. Numer. Methods Heat Fluid Flow **29**(8), 2524–2544 (2019)

Sun, Q., Pop, I.: Free convection in a triangle cavity filled with a porous medium saturated with nanofluids with flush mounted heater on the wall. Int. J. Therm. Sci. **50**, 2141–2153 (2011)
Tahmasebi, A., Mahdavi, M., Ghalambaz, M.: Local thermal nonequilibrium conjugate natural convection heat transfer of nanofluids in a cavity partially filled with porous media using Buongiorno's model. Numer. Heat Transf. Part A Appl. **73**, 254–276 (2018)
Tiari, S., Qiu, S., Mahdavi, M.: Numerical study of finned heat pipe-assisted thermal energy storage system with high temperature phase change material. Energy Convers. Manage. **89**, 833–842 (2015)
Wang, J., Gan, Y., Liang, J., Tan, M., Li, Y.: Sensitivity analysis of factors influencing a heat pipe-based thermal management system for a battery module with cylindrical cells. Appl. Therm. Eng. **151**, 475–485 (2019a)
Wang, S., Guo, Y., Peng, C., Wang, W.: Experimental study of paraffin melting in cylindrical cavity with central electric heating rod. J. Environ. Manage. **237**, 264–271 (2019b)
Zhao, B., Gain, A.K., Ding, W., Zhang, L., Li, X., Fu, Y.: A review on metallic porous materials: pore formation, mechanical properties, and their applications. Int. J. Adv. Manuf. Technol. **95**, 2641–2659 (2018)

Affiliations

S. A. M. Mehryan[1] · Kasra Ayoubi-Ayoubloo[2] · Mohammad Shahabadi[3] · Mohammad Ghalambaz[4,5] · Pouyan Talebizadehsardari[6,5] · Ali Chamkha[7]

1 Young Researchers and Elite Club, Yasooj Branch, Islamic Azad University, Yasooj, Iran

2 Department of Mechanical Engineering, Shahid Chamran University of Ahvaz, Ahvaz, Iran

3 Department of Mechanical Engineering, Isfahan University of Technology, Isfahan, Iran

4 Metamaterials for Mechanical, Biomechanical and Multiphysical Applications Research Group, Ton Duc Thang University, Ho Chi Minh City, Vietnam

5 Faculty of Applied Sciences, Ton Duc Thang University, Ho Chi Minh City, Vietnam

6 Department for Management of Science and Technology Development, Ton Duc Thang University, Ho Chi Minh City, Vietnam

7 Mechanical Engineering Department, Prince Mohammad Endowment for Nanoscience and Technology, Prince Mohammad Bin Fahd University, Al-Khobar 31952, Saudi Arabia